Int. J. Heat Mass Transfer. Vol. 35, No. 2, pp. 433–442, 1992
Printed in Great Britain

0017–9310/92 $5.00 + 0.00

Heat transfer and fluid flow in floating-zone crystal growth with a mostly covered melt surface

C. W. LAN and SINDO KOU

Department of Materials Science and Engineering and Center of Excellence in Solidification Processing Technologies of Engineering Materials, University of Wisconsin, Madison, WI 53706, U.S.A.

(*Received* 29 *May* 1990 *and in final form* 25 *February* 1991)

Abstract—Computer simulation was conducted to study a modified floating-zone crystal growth process, in which the melt surface is mostly covered with a heated ring. The growth of 6 mm diameter single crystals of $NaNO_3$ was considered, and the effects of the following parameters were studied: (1) temperature of the ring, (2) growth rate, (3) surface tension–temperature coefficient of the melt, (4) thermal expansion coefficient of the melt, and (5) gravity. It was demonstrated that thermocapillary convection in the melt zone is reduced significantly in this modified process. The model was checked against the measured lengths of the meniscus near the growth front and axial temperature distribution in a growing crystal, and the agreement was good.

INTRODUCTION

FIGURE 1(a) illustrates the crystal growth process which has been developed recently by modifying the conventional floating-zone process. As shown, a melt zone is produced in the feed rod by a heated ring and the ring covers most of the surface of the melt zone. The ring is an extension from the bottom of the disk, which is supported and heated by a resistance sheet heater. The sheet heater has a round hole to let the ring pass through. The thermocouple helps control heating of the ring during crystal growth. As the ring travels upward, the feed rod continues to melt and the crystal continues to grow. This modified process differs from the conventional floating-zone process mainly in that the surface of the melt zone in the latter is completely free.

The advantages of the modified process are as follows. First, the cross-sectional uniformity and surface smoothness of the resultant crystals are improved. Second, strong, oscillatory thermocapillary convection in the melt zone can be avoided. Third, when used under normal gravity, the stability of the melt zone is greater. The disadvantage, however, is that it is limited by the requirement of chemical compatibility between the melt and the ring. A recent survey by one of the authors [1] has indicated that crystals of many different materials can, in fact, be grown by this process.

In a recent study [2], $NaNO_3$ single crystals of 6 mm diameter were grown by the modified process. These crystals exhibited a very uniform diameter and smooth surface. The free surface near the growth front (i.e. the melt/crystal interface) was observed through a macrophoto camera system. It was observed that tiny impurity particles moved in a loop-like fashion near the free surface. These particles moved downward across the free surface, and upward back to the top of the free surface penetrating only slightly into the melt zone. The lengths of the free surface were measured from photographs taken during crystal growth. A K-type thermocouple of 0.13 mm wire diameter was placed at the centerline of the melt zone near the growth front. The axial temperature distribution in the crystal was measured as the growth front continued to advance beyond the thermocouple. It was also observed that the temperature of the ring was about 4°C lower at the bottom than at the top.

The purpose of the present study is to better understand this modified floating-zone process, through computer simulation of heat transfer and fluid flow in the melt zone. The effect of heat transfer and fluid flow on the unknown shapes of the melt/solid (i.e. melt/crystal and melt/feed) interfaces is of particular interest to us. Another modified floating-zone process was also simulated recently, in which the extension from the bottom of the disk is in the form of a round step and a small hole is located at the center of the disk/step [3]. Due to the small size of the hole, the melt/solid interfaces are essentially flat under normal crystal growth conditions and natural convection in the melt zone is negligible. As will be shown in the present study, the situation here is the opposite, i.e. the interfaces are rather convex and natural convection prevails in the bulk melt zone.

PHYSICAL SYSTEM AND PROPERTIES

Convection in the melt is considered to be steady, axisymmetrical, laminar and Newtonian. Temperature measurements indicated no temperature fluctuations due to oscillatory flow, thus suggesting steady-state flow in the melt. Since the melt of $NaNO_3$ is transparent, the melt/solid interfaces could be observed during crystal growth. The fact that these

NOMENCLATURE

C_p	specific heat
$\mathbf{e}_z$	unit vector in z-direction
g	gravitational acceleration
h	heat transfer coefficient
ΔH	heat of fusion per unit solid mass
k	thermal conductivity
$\mathbf{n}$	unit normal vector
r	cylindrical coordinate
R_0	radius of feed rod
T	temperature
T_a	ambient temperature
T_m	melting point
T_r	temperature of the ring
$T_{1/2}$	temperature far away from melt zone
u	r-component of velocity
U_0	pulling speed or growth rate
v	z-component of velocity
z	cylindrical coordinate.

Greek symbols

γ	surface tension
ε	emissivity
η	curvilinear coordinate
μ	viscosity
ξ	curvilinear coordinate
ρ	density
σ	Stefan–Boltzmann constant
ψ	stream function
ω	vorticity.

Subscripts

L	liquid or melt at melting point
S	solid.

interfaces were axisymmetrical suggests that the assumption of axisymmetry is reasonable. The free surfaces of the melt are assumed to be cylindrical. In reality, the free surface below the ring is very close to being exactly cylindrical. The free surface above the ring, on the other hand, is somewhat like a bell shape, as shown schematically in Fig. 1(a). Since this free surface is separated from the growth front by the ring, its exact shape is not expected to affect the resultant crystal significantly.

The relevant dimensions of the physical system are as follows. The feed rod, the outer surface of the ring and the single crystal are all 6 mm in diameter. The wall thickness and height of the aluminum ring are 0.5 and 3 mm, respectively. The physical properties of $NaNO_3$ are given in Table 1.

Table 1. Physical properties of $NaNO_3$ [4–7]

T_m	$= 306.8°C$
ΔH	$= 182\ J\ g^{-1}$
h	$= 9.0\times10^{-4}\ W\ cm^{-2}\ °C^{-1}$
k_S	$= 5.65\times10^{-3}+33.5(T-230)\times10^{-7}\ W\ cm^{-1}\ °C^{-1}$
k_L	$= 5.65\times10^{-3}+47.7(T-T_m)\times10^{-7}\ W\ cm^{-1}\ °C^{-1}$
$C_{\rho S}$	$= C_{\rho L} = 1.255+2.18(T-100)\times10^{-3}\ J\ g^{-1}\ °C^{-1}$
ε	$= 0.7$
β	$= 6.6\times10^{-4}\ °C^{-1}$
$\partial\gamma/\partial T$	$= -0.056\ dyne\ cm^{-1}\ °C^{-1}$
μ	$= 0.0302\text{–}1.533\times10^{-4}\ (T-T_m)\ g\ cm^{-1}\ s^{-1}$
ρ_S	$= 2.118\ g\ cm^{-3}$
ρ_L	$= 1.904\ g\ cm^{-3}$

GOVERNING EQUATIONS AND BOUNDARY CONDITIONS

The cylindrical coordinates (r, z) are shown in Fig. 1(b). For convenience, the ring and the coordinates are considered to be stationary, while the crystal and the feed rod are moving in the negative z-direction. The division of the physical system into one- and two-dimensional regions for heat transfer computation will be explained later.

The governing equations [8] are as follows.

Equation of motion

$$\frac{\partial}{\partial r}\left(\frac{\omega}{r}\frac{\partial\psi}{\partial z}\right)-\frac{\partial}{\partial z}\left(\frac{\omega}{r}\frac{\partial\psi}{\partial r}\right)+\frac{\partial}{\partial r}\left[\frac{1}{r}\frac{\partial}{\partial r}(\mu r\omega)\right]+\frac{\partial}{\partial z}\left[\frac{1}{r}\frac{\partial}{\partial z}(\mu r\omega)\right]-\rho_L\beta g\left(\frac{\partial T}{\partial r}\right)=0. \quad (1)$$

Stream equation

$$\frac{\partial}{\partial z}\left[\frac{1}{\rho_L r}\frac{\partial\psi}{\partial z}\right]+\frac{\partial}{\partial r}\left[\frac{1}{\rho_L r}\frac{\partial\psi}{\partial r}\right]+\omega=0. \quad (2)$$

Energy equation

$$\frac{\partial}{\partial r}\left(C_pT\frac{\partial\psi}{\partial z}\right)-\frac{\partial}{\partial z}\left(C_pT\frac{\partial\psi}{\partial r}\right)+\frac{\partial}{\partial z}\left(rk\frac{\partial T}{\partial z}\right)+\frac{\partial}{\partial r}\left(rk\frac{\partial T}{\partial r}\right)=0. \quad (3)$$

The stream function ψ and vorticity ω in the above equations are defined in terms of the radial velocity u and the axial velocity v as follows:

$$u=-\frac{1}{\rho_L r}\frac{\partial\psi}{\partial z},\quad v=\frac{1}{\rho_L r}\frac{\partial\psi}{\partial r} \quad (4)$$

$$\omega=\frac{\partial u}{\partial z}-\frac{\partial v}{\partial r}. \quad (5)$$

The thermal boundary conditions are as follows:

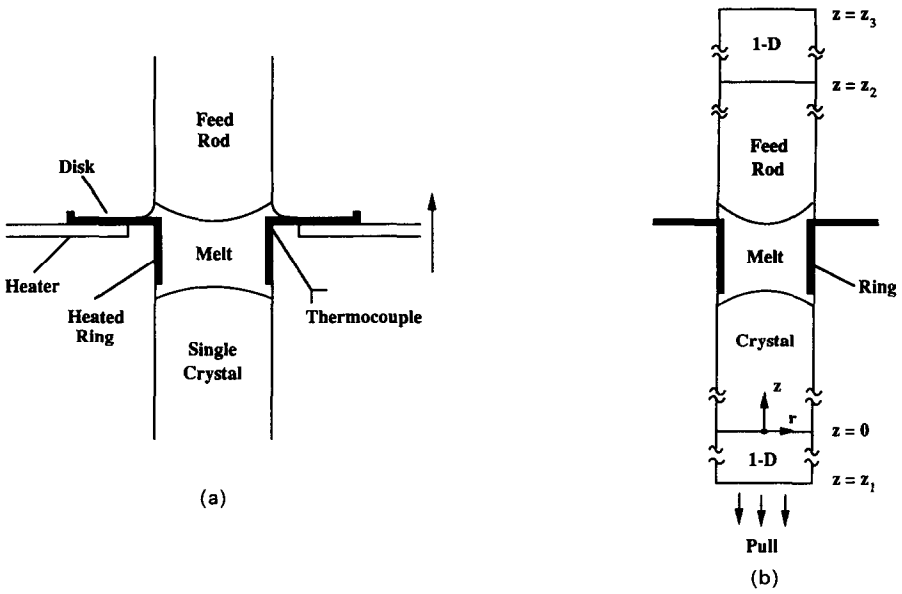

FIG. 1. A modified floating-zone crystal growth process in which a heated ring covers most of the surface of the melt zone. (a) Schematic illustration. (b) Division of the physical system into one- and two-dimensional regions to reduce the load of computation.

(1) Along the centerline of the system

$$\frac{\partial T}{\partial r} = 0 \quad \text{due to symmetry.}$$

(2) At the melt/ring interface

$$T = T_r$$

where T_r is the temperature of the heated ring. It is assumed to increase linearly from the bottom of the ring to the top.

(3) At the melt/solid interfaces

$$T = T_m$$

and

$$k(\mathbf{n}\cdot\nabla T)|_S - k(\mathbf{n}\cdot\nabla T)|_L + \rho_S \Delta H U_0 \mathbf{n}\cdot\mathbf{e}_z = 0$$

where $\mathbf{n}$ is the unit normal vector pointing into the melt.

(4) On the surfaces of the feed rod, melt and crystal

$$-k(\mathbf{n}\cdot\nabla T) = h(T - T_a) + \varepsilon\sigma(T^4 - T_a^4)$$

where $\mathbf{n}$ is the unit normal vector pointing radially outward.

(5) Far away from the melt zone

$$T = T_{1/2}.$$

$T_{1/2}$ is the temperature in the feed rod or crystal at a location far away from the melt zone. The implementation of this boundary condition will be described later in 'Method of Solution'.

The fluid-flow boundary conditions are as follows:

(1) Along the centerline of the melt zone

$$\psi = 0, \quad \omega = 0.$$

The stream function is set to zero at the centerline as a reference. The zero vorticity is the result of $\partial u/\partial z = \partial v/\partial r = 0$ at the centerline.

(2) At the melt/ring interface

$$\psi = \tfrac{1}{2}\rho_S U_0 R_0^2$$

$$\omega = \frac{\partial u}{\partial z} \quad \text{(horizontal portion)}$$

$$\omega = -\frac{\partial v}{\partial r} \quad \text{(vertical portion)}$$

where R_0 is the diameter of the crystal. The equation for ψ is obtained by integrating equation (4) with $v = U_0\rho_S/\rho_L$.

(3) At the melt/solid interfaces

$$\psi = \tfrac{1}{2}\rho_S U_0 r^2$$

$$\omega = \frac{\partial u}{\partial z} - \frac{\partial v}{\partial r}.$$

(4) On the free surface of the melt

$$\psi = \tfrac{1}{2}\rho_S U_0 R_0^2$$

$$\omega = -\frac{\partial v}{\partial r} = \frac{1}{\mu}\frac{\partial \gamma}{\partial T}\frac{\partial T}{\partial z}$$

where $\partial\gamma/\partial T$ is the surface tension–temperature coefficient of the melt.

COORDINATE TRANSFORMATION

Due to the fact that the melt/solid interface is not flat but is curved, the Stefan condition and the vor-

ticity boundary condition in terms of the cylindrical coordinate system (r, z), i.e. Thermal Boundary Condition 3 and Fluid-flow Boundary Condition 3, cannot be properly implemented. In view of this, we have transformed the above governing equations and boundary conditions into those in terms of general (nonorthogonal) curvilinear coordinates (η, ξ) which fit all the physical boundaries including the melt/solid interface. In this way, all the boundary conditions can be treated accurately.

Following the procedure of Thompson *et al.* [9], equations (1), (2) and (3) can be transformed into the following general form:

$$\frac{\partial}{\partial\eta}\left(a\phi\frac{\partial\psi}{\partial\xi}\right)-\frac{\partial}{\partial\xi}\left(a\phi\frac{\partial\psi}{\partial\eta}\right)+\frac{b}{J}\left[g_{22}\frac{\partial^2(c\phi)}{\partial\eta^2}+g_{11}\frac{\partial^2(c\phi)}{\partial\xi^2}\right]+d_{PQ}+d_{\text{nor}}+d_{\text{or}}=0. \quad (6)$$

Coefficients a, b, c and d in the above equation are given in Table 2 for $\phi=\psi$, ω and T, respectively. Other coefficients in the same equation are defined as follows:

$$d_{PQ}=bJ\left[P(\eta,\xi)\frac{\partial(c\phi)}{\partial\eta}+Q(\eta,\xi)\frac{\partial(c\phi)}{\partial\xi}\right]$$

$$d_{\text{nor}}=-\frac{2bg_{12}}{J}\frac{\partial^2(c\phi)}{\partial\eta\,\partial\xi}+\frac{1}{J}\left[\left(g_{22}\frac{\partial b}{\partial\eta}-g_{12}\frac{\partial b}{\partial\xi}\right)\frac{\partial(c\phi)}{\partial\eta}+\left(g_{11}\frac{\partial b}{\partial\xi}-g_{12}\frac{\partial b}{\partial\eta}\right)\frac{\partial(c\phi)}{\partial\xi}\right]$$

$$d_{\text{or}}=Jd$$

$$g_{11}=\left(\frac{\partial r}{\partial\eta}\right)^2+\left(\frac{\partial z}{\partial\eta}\right)^2$$

$$g_{22}=\left(\frac{\partial r}{\partial\xi}\right)^2+\left(\frac{\partial z}{\partial\xi}\right)^2$$

$$g_{12}=\left(\frac{\partial r}{\partial\eta}\right)\left(\frac{\partial r}{\partial\xi}\right)+\left(\frac{\partial z}{\partial\eta}\right)\left(\frac{\partial z}{\partial\xi}\right)$$

$$J=\left(\frac{\partial r}{\partial\eta}\right)\left(\frac{\partial z}{\partial\xi}\right)-\left(\frac{\partial z}{\partial\eta}\right)\left(\frac{\partial r}{\partial\xi}\right)$$

$$P=-\left(\frac{\partial^2 r}{\partial\eta^2}\right)\Big/\left(\frac{\partial r}{\partial\eta}\right)^3$$

$$Q=-\left\{\left(\frac{\partial z}{\partial\xi}\frac{\partial z}{\partial\eta}\frac{\partial^2 r}{\partial\eta^2}-\frac{\partial z}{\partial\xi}\frac{\partial r}{\partial\eta}\frac{\partial^2 z}{\partial\eta^2}\right)+2\left(\frac{\partial r}{\partial\eta}\frac{\partial z}{\partial\eta}\frac{\partial^2 z}{\partial\eta\,\partial\xi}\right)-g_{11}\left(\frac{\partial r}{\partial\eta}\frac{\partial^2 z}{\partial\xi^2}\Big/\frac{\partial z}{\partial\xi}\right)\right\}\Big/\left[\left(\frac{\partial r}{\partial\eta}\right)^3\left(\frac{\partial z}{\partial\xi}\right)^2\right].$$

The transformed thermal boundary conditions are as follows:

(1) Along the centerline of the system

$$\frac{\partial T}{\partial\eta}=0.$$

Table 2. Coefficients a, b, c and d in equation (6)

ϕ	a	b	c	d
ψ	0	$\frac{1}{\rho_L r}$	1	ω
ω	$\frac{1}{r}$	$\frac{1}{r}$	μr	$-\frac{\rho_L g\beta}{J}\left[\frac{\partial z}{\partial\xi}\frac{\partial T}{\partial\eta}-\frac{\partial z}{\partial\eta}\frac{\partial T}{\partial\xi}\right]$
T	C_p	kr	1	0

(2) At the melt/ring interface

$$T=T_r.$$

(3) At the melt/solid interfaces

$$T=T_m$$

and

$$k(\mathbf{n}\cdot\nabla T)|_S-k(\mathbf{n}\cdot\nabla T)|_L+\rho_S\Delta H U_0\mathbf{n}\cdot\mathbf{e}_z=0.$$

(4) On the surfaces of the feed rod, melt and crystal

$$-k(\mathbf{n}\cdot\nabla T)=h(T-T_a)+\varepsilon\sigma(T^4-T_a^4).$$

(5) Far away from the melt zone

$$T=T_{1/2}.$$

The transformed fluid-flow boundary conditions are as follows:

(1) Along the centerline of the melt zone

$$\psi=0,\quad \omega=0.$$

(2) At the melt/ring interface

$$\psi=\tfrac{1}{2}\rho_S U_0 R_0^2$$

$$\omega=-\frac{g_{11}}{\rho_L r J^2}\frac{\partial^2\psi}{\partial\xi^2}\quad\text{(horizontal portion)}$$

$$\omega=-\frac{g_{22}}{\rho_L r J^2}\frac{\partial^2\psi}{\partial\eta^2}\quad\text{(vertical portion)}.$$

(3) At the melt/solid interfaces

$$\psi=\tfrac{1}{2}\rho_S U_0 r^2$$

$$\omega=-\frac{g_{11}}{\rho_L r J^2}\frac{\partial^2\psi}{\partial\xi^2}.$$

(4) On this free surface of the melt

$$\psi=\tfrac{1}{2}\rho_S U_0 R_0^2$$

$$\omega=-\frac{1}{\mu g_{22}^{1/2}}\frac{\partial\gamma}{\partial T}\frac{\partial T}{\partial\xi}.$$

METHOD OF SOLUTION

The grid spacing in the physical domain is non-uniform, i.e. being finer near the melt/solid and melt/air interfaces in order to treat the higher velocity and temperature gradients at these locations more accurately. The grid spacing in the computational (i.e.

transformed) domain, however, is uniform with $\Delta\eta = \Delta\xi =$ constant. In this way, second order accuracy is retained in the finite difference approximations. Furthermore, a special procedure has been used in grid generation to ensure that $\partial z/\partial\xi$ is continuous at both ξ_t and ξ_b, where ξ_t and ξ_b are the values of ξ at the top and bottom of the ring, respectively. In this way, $\partial z/\partial\xi$ can be determined accurately at both ξ_t and ξ_b.

In order to reduce the load of computation, the material being considered is divided into three regions (Fig. 1(b)), i.e. an inner region which consists of the melt zone and the solid material near the melt/solid interfaces, an outer region in the crystal and an outer region in the feed rod. Heat transfer is considered to be two-dimensional in the inner region, but is approximated as one-dimensional in the outer ones. The inner region is made long enough so that the two-dimensional temperature distribution in this region becomes essentially one-dimensional (i.e. uniform in the radial direction) at its two ends. For the present problem involving a small radius (e.g. $R_0 = 0.3$ cm), we find a length of about $35R_0$ to be sufficient; further length increases produce no significant changes. In the two outer regions, which are ten times longer than the inner one, heat transfer is described by the following equation:

$$-U_0\rho_s C_p\frac{dT}{dz}+\frac{d}{dz}\left(k\frac{dT}{dz}\right)-\frac{2}{R_0}[h(T-T_a)+\sigma\varepsilon(T^4-T_a^4)]=0. \quad (7)$$

Heat flow from the inner region across the boundary at $z = 0$ or z_2 into the outer region can be described as follows:

$$-k\int_0^{R_0}\left.\frac{\partial T}{\partial z}\right|_{z=0^+\text{ or }z_2^-}\cdot 2\pi r\,dr = -k\left.\frac{dT}{dz}\right|_{z=0^-\text{ or }z_2^+}\cdot\pi R_0^2. \quad (8)$$

From the result of heat flow computation in the inner region, the LHS of equation (8) can be calculated. The temperature gradients dT/dz at $z = 0$ and dT/dz at $z = z_2$, along with $dT/dz = 0$ at both z_1 and z_3, are used as boundary conditions for solving equation (7) in the outer regions. The newly calculated temperatures at $z = 0$ and z_2, i.e. $T_{1/2}$ in Thermal Boundary Condition 5, are then used as updated boundary conditions for the next iteration of heat flow computation in the inner region. This procedure is repeated until the temperature field converges. A similar overall approach has been used by Duranceau and Brown [10] for conduction heat-flow computation in conventional floating-zone crystal growth.

The numerical method used in the present study is similar to that described elsewhere [11] and hence will not be repeated here.

RESULTS AND DISCUSSION

Figure 2(a) shows a portion of a grid system used for computation. This grid system, like all other grid systems in this study, was updated each time the melt/solid interfaces were updated during computation. As shown, the grid spacing is finer near all melt/solid and melt/air interfaces. The mesh is 21×21 in the feed rod, 21×66 in the melt zone (and the ring), and 21×21 in the crystal. A similar but finer grid system is shown in Fig. 2(b), where the mesh is 41×21 in the feed rod, 41×81 in the melt zone (and the ring), and 41×21 in the crystal. The calculated results based on the grid systems in Figs. 2(a) and (b) are shown in Figs. 3(a) and (b), respectively. A secondary flow loop about two orders of magnitude weaker than the surface flow loops is shown in Fig. 3(b) near the upper inner corner of the ring. The asterisk indicates that the stream function of the flow line is zero. Although this secondary flow loop is not shown in Fig. 3(a), the calculated results in Figs. 3(a) and (b) are still very close to each other. Therefore, we have chosen to use the coarser grid system for all cases of computation, except for the case of a higher ring temperature (Fig. 5) where the free surface is longer.

Figure 3(a) shows the calculated result for a crystal growing with a ring whose temperature varies linearly from 321°C at the bottom to 325°C at the top. This temperature distribution will be used throughout the present study, unless otherwise stated. The growth rate is 5.2 mm h^{-1}, i.e. $U_0 = -5.2$ mm h^{-1}. This ring temperature and growth rate were used to grow a 6 mm diameter single crystal of $NaNO_3$. The two flow loops near the free surface are due to thermocapillary convection. In other words, thermocapillary convection is limited to very near the free surface. This is significantly different from the case of conventional floating-zone crystal growth, where thermocapillary convection can penetrate deep into the melt zone [12]. Since $\partial\gamma/\partial T$ is negative, the upper loop is clockwise while the lower is counterclockwise. At the center of the upper loop the stream function is at its minimum, i.e. $\psi_{min} = -5.95\times10^{-3}$ g s^{-1}, while at the center of the lower loop the stream function is at its maximum, i.e. $\psi_{max} = 3.37\times10^{-3}$ g s^{-1}. The increment in the value of the stream function, i.e. $\Delta\psi$, is 5.0×10^{-4} g s^{-1}. The fastest surface velocities are $v_{max} = 2.37$ cm s^{-1} and $v_{min} = -2.26$ cm s^{-1} for the upper and lower loops, respectively. Since the surface flow is directed toward the melt/solid interfaces, the portions of the isotherms near the free surface are pushed toward these interfaces, resulting in melting back of both the feed rod and the crystal near the free surface.

The flow loop inside the ring is due to natural convection. The melt near the inner wall of the ring is heated by the ring. Due to thermal expansion it floats up, producing a clockwise natural convection loop. At the center of the loop the stream function is at its minimum, i.e. $\psi_{min} = -2.32\times10^{-3}$ g s^{-1}. The fastest velocity is $v_{min} = -0.207$ cm s^{-1} and is located at the centerline.

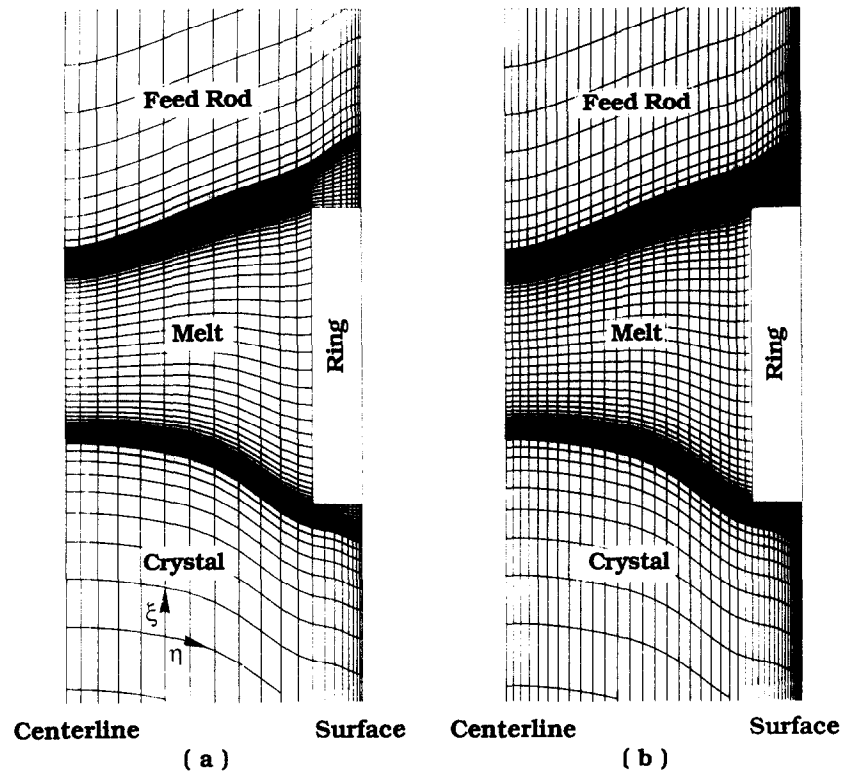

FIG. 2. Grid systems used for computation. (a) A portion of a coarser grid system. (b) A portion of a finer grid system.

The isotherms are shown with an increment of $\Delta T = (T_t - T_m)/5$ in both the melt and solid, where T_t is the temperature at the top of the ring. The same definition of ΔT will be used throughout the rest of this report.

The calculated length of the free surface near the growth front is 0.41 mm. Due to this rather small length, we were unable to measure the surface velocities during crystal growth. However, from the close-up photographs, the length of the free surface near the growth front was found to be about 0.43 mm. The calculated value of 0.41 mm, therefore, appears to be in good agreement with the observed one. As already mentioned, tiny impurity particles were observed to move downward across the free surface, from the bottom of the ring to the growth front. These particles then moved upwards back to the bottom of the ring in a loop-like fashion, penetrating only slightly into the melt. The calculated thermocapillary flow pattern near the growth front is consistent with this observation. The calculated axial temperature distribution along the crystal is also in good agreement with the measured one, as shown in Fig. 4.

Effect of ring temperature

Figure 5 shows the calculated result for a crystal growing with a ring whose temperature varies linearly from 325°C at the bottom to 328°C at the top. The growth rate is 5.2 mm h^{-1}. This ring temperature and growth rate were also used to grow a 6 mm diameter single crystal of $NaNO_3$. The two flow loops near the free surface are similar to those shown previously in Fig. 3(a) but significantly stronger. At the center of the upper loop $\psi_{min} = -1.17 \times 10^{-2}$ g s^{-1}, while at the center of the lower loop $\psi_{max} = 6.16 \times 10^{-3}$ g s^{-1}. The fastest surface velocities are $v_{max} = 2.29$ cm s^{-1} and $v_{min} = -2.24$ cm s^{-1} for the upper and lower loops, respectively. These velocities are close to those in the case of Fig. 3(a). Due to the higher ring temperature, the natural convection loop inside the ring is also stronger, ψ_{min} being -3.34×10^{-3} g s^{-1}. Due to the stronger thermocapillary and natural convection, the isotherms are rather distorted.

The average zone length is greater than that shown in Fig. 3(a). The calculated length of the free surface near the growth front is 0.80 mm, which is in good agreement with the observed value of about 0.81 mm.

Effect of growth rate

Figure 6 shows the calculated result for a crystal growing with a five times faster rate of 26 mm h^{-1}. As compared to Fig. 3(a), the growth front becomes less convex, while the melting front is more convex. Also, the overall position of the melt zone shifts downward. The stream functions are $\psi_{min} = -4.42 \times 10^{-3}$ g s^{-1} and $\psi_{max} = 4.18 \times 10^{-3}$ g s^{-1} at the centers of the upper and lower surface flow loops, respectively. The surface velocities are $v_{max} = 2.55$ cm s^{-1} and $v_{min} = -2.07$ cm s^{-1} for the upper and lower surface flow loops, respectively. A very small flow loop is

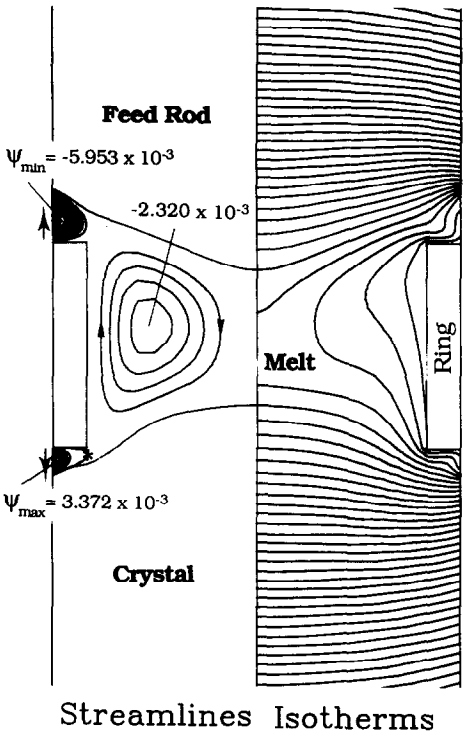

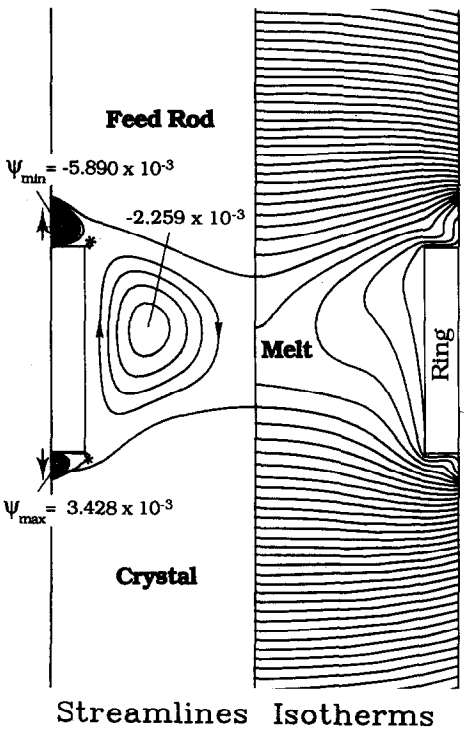

FIG. 3. Calculated results based on two different grid systems. (a) The coarser grid system in Fig. 2(a). (b) The finer grid system in Fig. 2(b).

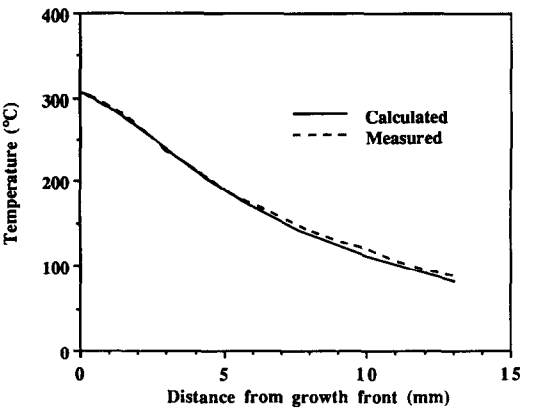

FIG. 4. Calculated and measured temperature distributions along the axis of a growing crystal.

induced by the upper surface-flow loop and is counter-clockwise in direction.

Effect of surface tension–temperature coefficient

Figures 7(a) and (b) show the calculated results for two less negative values of $\partial\gamma/\partial T$, i.e. -0.028 and 0 dyne cm^{-1} °C^{-1}, respectively. The growth rate is 5.2 mm h^{-1}. In Fig. 7(a) the two flow loops near the free surface are significantly weaker than those shown previously in Fig. 3(a) for $\partial\gamma/\partial T$ equal to -0.056 dyne cm^{-1} °C^{-1}. At the center of the upper loop $\psi_{min} = -2.93 \times 10^{-3}$ g s^{-1}, while at the center of the lower loop $\psi_{max} = 1.92 \times 10^{-3}$ g s^{-1}. The fastest surface velocities are $v_{max} = 1.59$ cm s^{-1} and

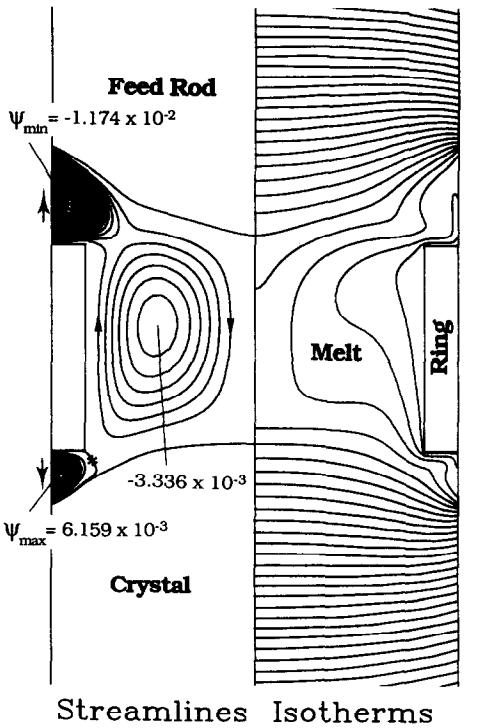

FIG. 5. Calculated result based on a ring temperature higher than that in Fig. 3.

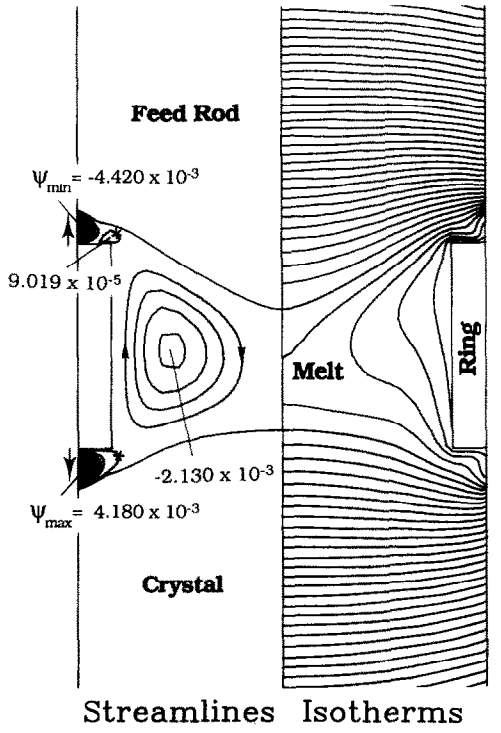

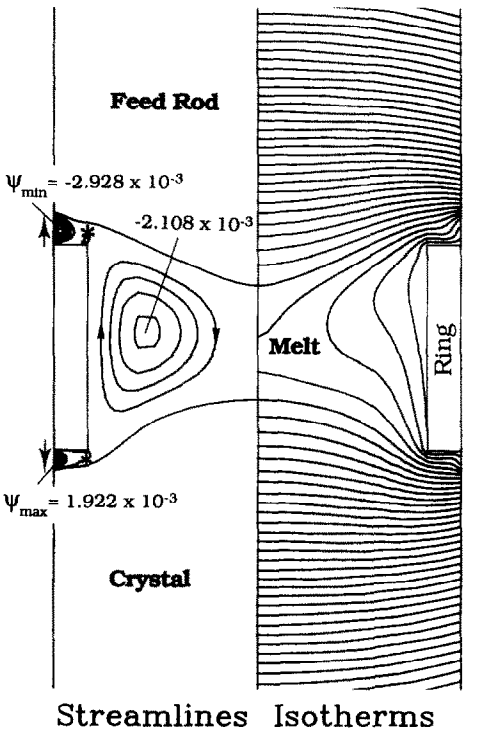

FIG. 6. Calculated result based on a growth rate which is five times that in Fig. 3(a).

$v_{min} = -1.52$ cm s^{-1} for the upper and lower loops, respectively. This weaker thermocapillary convection results in a melt zone which is shorter than that in Fig. 3(a). In Fig. 7(b) there are no longer any thermocapillary flow loops. The two very weak flow loops near the free surface are induced by the natural convection loop inside the ring, both being counterclockwise in direction and of the order of 10^{-5} g s^{-1}. Due to the absence of thermocapillary convection, the melt/solid interfaces no longer melt back near the free surface.

The calculated temperature gradients in the melt at and normal to the growth front ($\partial T/\partial n$) are shown in Fig. 8 as a function of radius and $\partial\gamma/\partial T$. Away from the free surface $\partial T/\partial n$ is insensitive to the variation in $\partial\gamma/\partial T$. Near the free surface, however, the opposite is true. Without thermocapillary convection ($\partial\gamma/\partial T = 0$), the isotherms near the free surface are essentially parallel to the growth front. The slight increase in $\partial T/\partial n$ near the free surface is due to surface heat losses. With strong thermocapillary convection ($\partial\gamma/\partial T = -0.056$ dyne cm^{-1} $°C^{-1}$), however, the surface flow pattern is such that the portion of the isotherms very close to the free surface is pushed against the growth front, but the portion slightly away from the free surface is pulled away from it. Consequently, the maximum $\partial T/\partial n$ is located at the free surface and a minimum $\partial T/\partial n$ exists just slightly away from the free surface. Since heat transfer to the local growth front is proportional to the local $\partial T/\partial n$, the local growth front very close to the free surface is melted back, as shown in Fig. 3(a). On the contrary, a very

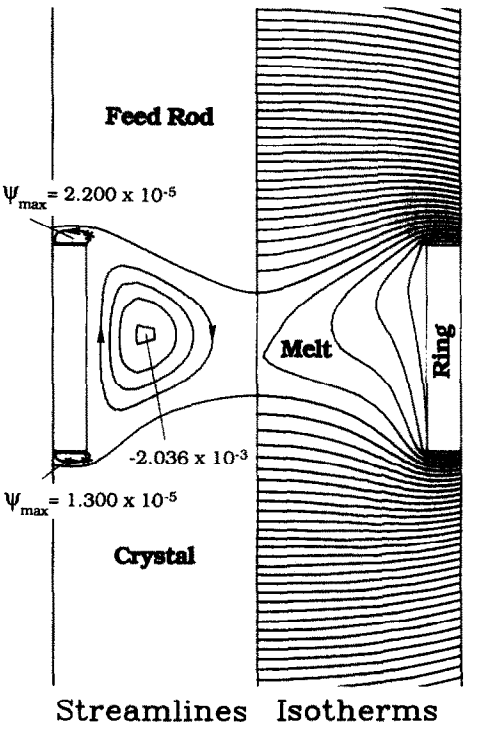

FIG. 7. Calculated results based on reduced values of $\partial\gamma/\partial T$. (a) -0.028 dyne cm^{-1} $°C^{-1}$. (b) 0 dyne cm^{-1} $°C^{-1}$.

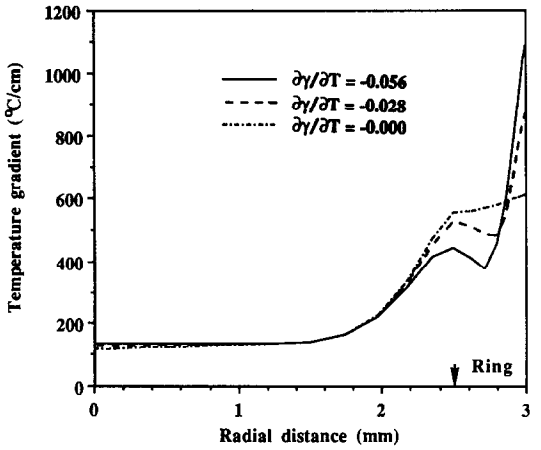

FIG. 8. Calculated temperature gradients in the melt at and normal to the growth front as a function of radius for three different levels of $\partial\gamma/\partial T$.

small hump forms on the growth front just slightly away from the free surface.

Effect of thermal expansion coefficient

Figure 9 shows the calculated result for the case where the thermal expansion coefficient of the melt, β, is doubled. As shown, the natural convection loop inside the ring is significantly stronger than that shown previously in Fig. 3(a), ψ_{min} being -3.98×10^{-3} g s^{-1} at the center of the loop. As compared to Fig. 3(a), the length of the melt zone is essentially the same near the free surface, but significantly larger near the centerline. It appears that due to the stronger natural convection, heat transfer from the ring to the centerline of the melt zone is improved significantly.

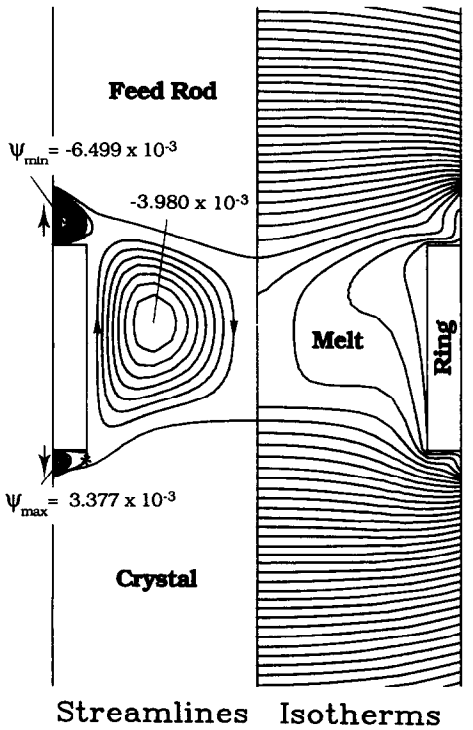

FIG. 9. Calculated result based on a thermal expansion coefficient which is twice that in Fig. 3(a).

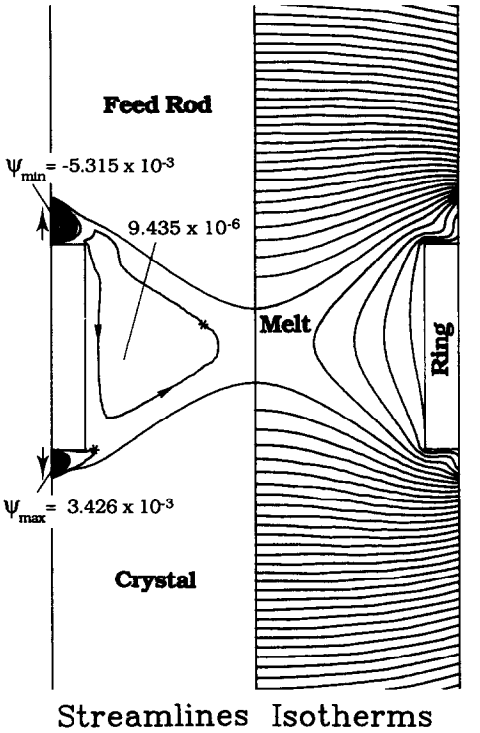

FIG. 10. Calculated result based on a zero gravitational acceleration.

Effect of gravity

Figure 10 shows the calculated result for the case where the gravitational acceleration, g, is reduced to zero, which is equivalent to crystal growth under the microgravity condition. As shown, natural convection no longer exists in the melt zone. The very weak flow loop inside the ring is induced by the upper surface flow loop, and is counterclockwise in direction, the stream function at the center of the loop being $\psi_{max} = 9.4 \times 10^{-6}$ g s^{-1}. Due to the absence of natural convection in the melt, the melting and growth fronts become more like the mirror image of each other. As compared to Fig. 3(a), the zone length is essentially the same near the free surface, but significantly shorter near the centerline. Due to the absence of natural convection, heat transfer from the ring to the centerline of the melt zone is by conduction only. To avoid freezing at the centerline, either the length or the temperature of the ring should be increased.

CONCLUSIONS

Computer simulation has been conducted to study heat transfer and fluid flow in the melt zone in a modified floating-zone crystal growth process, in which a heated ring covers most of the surface of the melt zone. The conclusions are as follows:

(1) The computer model agrees well with the observed lengths of the free surface near the growth

front, and the measured axial temperature distribution in a crystal.

(2) Thermocapillary convection is limited to near the free surface of the melt zone, and is significantly weaker than that in the conventional floating-zone process.

(3) Both thermocapillary convection and natural convection increase with increasing temperature of the ring.

(4) The length of the melt zone at its centerline is affected significantly by the extent of natural convection inside the ring. This length is significantly reduced under microgravity.

Acknowledgement—This work was supported by NASA under contract NAG8-705.

REFERENCES

1. S. Kou, Unpublished research, University of Wisconsin, Madison, Wisconsin (1989).
2. C. W. Lan and S. Kou, Floating-zone crystal growth with a heated ring covering the melt surface, *J. Crystal Growth* **108,** 1–7 (1991).
3. C. W. Lan and S. Kou, Floating-zone crystal growth with a heated step immersed in the melt—computer simulation, *J. Crystal Growth* **108,** 340–350 (1991).
4. L. R. White and H. T. Davis, Thermal conductivity of molten alkali nitrates, *J. Chem. Phys.* **47,** 5433–5439 (1967).
5. G. J. Janz, Properties of nitrates, nitrites, and mixtures, *J. Phys. Chem. Ref. Data* **1,** 583–624 (1972).
6. F. Preisser, D. Schwabe and A. Scharmann, Steady and oscillatory thermocapillary convection in liquid columns with free cylindrical surface, *J. Fluid Mech.* **126,** 545–567 (1983).
7. J. R. Welty, C. E. Wicks and R. E. Wilson, *Fundamentals of Momentum, Heat and Mass Transfer* (2nd Edn), pp. 353–362. Wiley, New York (1976).
8. A. D. Gosman, W. M. Pan, A. K. Runchal, D. B. Spalding and M. Wolfshtein, *Heat and Mass Transfer in Recirculating Flows*, pp. 18–115. Academic Press, London (1969).
9. J. F. Thompson, F. C. Thames and C. W. Mastin, Boundary-fitted curvilinear coordinate for solution of partial differential equations on fields containing any number of arbitrary 2-dimensional bodies. NASA Report: NASA-CR-2729 (July 1977).
10. J. L. Duranceau and R. A. Brown, A thermal-capillary model for the floating zone crystal growth process, *J. Crystal Growth* **75,** 367–389 (1986).
11. C. W. Lan and S. Kou, Thermocapillary flow and natural convection in a melt column with an unknown melt/solid interface, *Int. J. Numer. Meth. Fluids* **12,** 59–80 (1991).
12. C. W. Lan and S. Kou, Thermocapillary flow and melt/solid interfaces in floating-zone crystal growth under microgravity, *J. Crystal Growth* **102,** 1043–1058 (1990).

TRANSFERT THERMIQUE ET MOUVEMENT FLUIDE DANS LA CROISSANCE D'UNE ZONE CRISTALLINE FLOTTANTE AVEC UNE SURFACE DE BAIN PARTIELLEMENT COUVERTE

Résumé—On conduit une simulation numérique du mécanisme de croissance d'une zone cristalline flottante, dans laquelle la surface du bain est partiellement couverte par un anneau chauffé. On considère la croissance de cristaux uniques de $NaNO_3$, de 6 mm de diamètre, et les effets des paramètres suivants sont étudiés : (1) température de l'anneau, (2) vitesse de croissance, (3) coefficient de température de la tension interfaciale du bain, (4) coefficient de dilatation thermique du bain et (5) pesanteur. On montre que la convection thermocapillaire dans la zone fondue est significativement réduite dans ce mécanisme modifié. Le modèle est favorablement testé par les longueurs mesurées du ménisque près du front de croissance et par la distribution de température dans le cristal.

WÄRMEÜBERGANG UND STRÖMUNG BEIM WACHSTUM SCHWEBENDER KRISTALLE MIT GRÖSSTENTEILS BEDECKTER OBERFLÄCHE DER SCHMELZE

Zusammenfassung—Mit Hilfe einer Rechnersimulation wird ein modifizierter Prozeß des Wachstums schwebender Kristalle untersucht, bei dem die Oberfläche der Schmelze größtenteils mit einem beheizten Ring bedeckt ist. Es wird das Wachstum eines $NaNO_3$-Einkristalls (Durchmesser 6 mm) betrachtet. Der Einfluß folgender Parameter wird untersucht: (1) Temperatur des Rings, (2) Wachstumsgeschwindigkeit, (3) Temperaturkoeffizient der Oberflächenspannung der Schmelze, (4) thermischer Ausdehnungskoeffizient der Schmelze und (5) Schwerkraft. Es wird gezeigt, daß die durch Kapillarkräfte angetriebene Konvektion in der Schmelzzone signifikant durch dieses Verfahren verringert wird. Das Modell wird anhand von Meßdaten für die Länge des Meniskus in der Nähe der Wachstumsfront sowie die axiale Temperaturverteilung in einem wachsenden Kristall verglichen, wobei sich gute Übereinstimmung ergibt.

ТЕПЛОПЕРЕНОС И ТЕЧЕНИЕ ЖИДКОСТИ ПРИ РОСТЕ КРИСТАЛЛА В ЗОНЕ ФЛОТАЦИИ С ПОЧТИ ПОЛНОСТЬЮ ПОКРЫТОЙ ПОВЕРХНОСТЬЮ РАСПЛАВА

Аннотация—Проведено моделирование на ЭВМ модифицированного процесса роста кристалла в зоне флотации, при котором поверхность расплава почти полностью покрыта нагретым кольцом. Рассматривались рост единичных кристаллов $NaNO_3$ диаметром 6 мм, а также влияние на процесс следующих параметров: (1) температуры кольца, (2) скорости роста кристалла, (3) коэффициента поверхностного натяжения расплава, (4) коэффициента теплового расширения расплава и (5) силы тяжести. Показано, что при данном модифицированном процессе термокапиллярная конвекция в зоне расплава существенно уменьшается. Получено хорошее согласие между результатами предложенной модели и измеренными длинами мениска вблизи фронта роста и аксиальным распределением температур в растущем кристалле.